International Journal of Solids and Structures 102–103 (2016) 30–43

Contents lists available at ScienceDirect

International Journal of Solids and Structures

journal homepage: www.elsevier.com/locate/ijsolstr

Identification of nonlinear kinematic hardening constitutive model parameters using the virtual fields method for advanced high strength steels

Jiawei Fu[a], Frédéric Barlat[a], Jin-Hwan Kim[a,*], Fabrice Pierron[b]

[a] Graduate Institute of Ferrous Technology, Pohang University of Science and Technology, Pohang, Gyeongbuk 790-784, Republic of Korea
[b] Faculty of Engineering and the Environment, University of Southampton, Southampton SO17 1BJ, UK

ARTICLE INFO

Article history:
Received 13 June 2016
Revised 12 September 2016
Available online 21 October 2016

Keywords:
Nonlinear kinematic hardening
The virtual fields method
Parameter identification
Bauschinger effect
Advanced high strength steels

ABSTRACT

In this work, the nonlinear kinematic hardening combined with Voce isotropic hardening was selected to characterize the material behavior of advanced high strength steel sheet samples subjected to a few reverse loading cycles. Multi-components of backstress were considered for the combined nonlinear kinematical hardening model, namely, one, two, and three backstress components. To calibrate the model, an inverse problem solution tool, so-called virtual fields method, which takes full advantage of full-field deformation measurement, was applied to identify the material constitutive parameters. First, finite element simulations of forward-reverse simple shear were performed to validate the proposed identification method. The influence of strain noise on the identification accuracy was also evaluated. Then, the proposed method was applied to three kinds of sheet metals (DP600, TRIP780 and TWIP980) tested under two cycles of forward-reverse simple shear for parameter identification. The identification results obtained with different number of backstress components were critically discussed.

© 2016 Elsevier Ltd. All rights reserved.

1. Introduction

In the automotive industry, the material selection for automotive parts is driven by key factors such as safety and fuel efficiency. To meet these requirements, automotive parts need to be superior in strength and lightweighting. Advanced high strength steels (AHSS) exhibit improved strength and maintain high ductility compared to conventional steels or other lightweight materials. This allows a reduction in the use of materials while the performance requirements are still met, namely a high strength-to-weight ratio. Currently, AHSS are widely utilized for automotive applications. As is well known, springback is a short-coming for materials that have low strength-to-modulus ratio, which results in undesired shape after the release of load (Lee et al., 2005a, b; Narasimhan and Lovell, 1999), commonly seen for AHSS (Chongthairungruang et al., 2012; Oliveira et al., 2007; Zang et al., 2014). In order to predict the springback behavior, an effective way is to develop finite element (FE) simulation with proper material constitutive model.

Springback is closely related to the Bauschinger effect, which describes the decrease in yield stress and associated transient hardening phenomena after reloading in the reverse direction. Various models have been developed over the years to describe the Bauschinger effect since the isotropic hardening rule is not able to capture it. Among these models, kinematic hardening has been most exclusively employed. The early form that was specifically proposed to represent the Bauschinger effect presumes the yield surface translates in stress space while its shape is maintained (Prager, 1949; Ziegler, 1959). Later on, more comprehensive nonlinear kinematic hardening models that combine both translation and expansion of the yield surface were developed and found to be suitable for the prediction of material behavior under cyclic loading conditions (Chaboche, 1986; Dafalias and Popov, 1975; Frederick and Armstrong, 2007; Ohno and Wang, 1993; Yoshida and Uemori, 2002). More recently, further improvements have been made to account for material anisotropy (Chung et al., 2005; Geng and Wagoner, 2002; Lee et al., 2007; Yoshida et al., 2015). A general review for the kinematic hardening rules can be found in Chaboche (2008). As an alternative, another type of hardening rule based on distortional plasticity, so called homogeneous anisotropic hardening (HAH) (Barlat et al., 2011; Barlat et al., 2013; Barlat et al., 2014; Manopulo et al., 2015), assumes that the yield surface flattens on the opposite side of the active stress while expanding isotropically. This model was proposed to comprehensively describe the material anisotropy, Bauschinger and latent effects.

* Corresponding author.
E-mail addresses: jiaweifu@postech.ac.kr (J. Fu), f.barlat@postech.ac.kr (F. Barlat), jinkim@postech.ac.kr (J.-H. Kim), F.Pierron@soton.ac.uk (F. Pierron).

http://dx.doi.org/10.1016/j.ijsolstr.2016.10.020
0020-7683/© 2016 Elsevier Ltd. All rights reserved.

The identification of constitutive parameters for a given model is a key issue for the prediction of material behavior, e.g., in FE simulations. In practice, a direct determination of material parameters is difficult for a complex model since it requires a large number of simple determinate tests, added the fact that some parameters may not have a physical meaning. In this case, an inverse solution tool becomes highly desirable. There have been various inverse solution tools suitable for parameter identification as reviewed by Avril et al. (2008), for instance, finite element model updating (FEMU) (Farhat and Hemez, 1993; Güner et al., 2012; Roux and Bouchard, 2015; Zhang et al., 2014) and the virtual fields method (VFM) (Chalal et al., 2006; Grédiac and Pierron, 2006; Notta-Cuvier et al., 2013; Pierron and Grediac, 2012; Pierron et al., 2010b). These methods take advantage of the full-field deformation measurement techniques such as digital image correlation (DIC) (Sutton et al., 2009), the grid method (Grédiac et al., 2016), moiré and speckle interferometry (Creath, 1985; Post and Baracat, 1981), from which more comprehensive information of material behavior can be extracted from a greater number of measurement points on the specimen surface.

FEMU is based on updating a FE model with respect to the unknown parameters through minimizing the difference between the FE predictions and the experimental measurements in form of displacements, strains and/or forces. It has received attention for many years and, currently, is the primary approach for parameter identification of kinematic hardening models such as in Broggiato et al. (2008), Collin et al. (2009), Eggertsen and Mattiasson (2010), Omerspahic et al. (2006), Yin et al. (2012), Yoshida et al. (2003), Zang et al. (2014), Zhao and Lee (2002). In Rezaiee-Pajand and Sinaie (2009), a systematic mathematic approach was developed to calibrate the nonlinear kinematic hardening (NLKH) parameters by deriving the relation between the evolution of backstress and the plastic strain. A multi-set of nonlinear equations was established and then, the obtained equations were solved to determine the required parameters using an iterative technique such as Newton-Raphson approach. In other studies (Chaparro et al., 2008; Mahmoudi et al., 2011), genetic algorithm (GA) was used to minimize the difference between the numerical predictions and the experimental results when calibrating the NLKH models. However, FEMU has a drawback that it is time-consuming due to the iterative nature of the FE model updating process. The VFM, which is based on the principle of virtual work, on the other hand, takes full advantage of the strain maps measured with, e.g., DIC. A cost function that measures the gap between the total internal virtual work and the external virtual work is built up and minimized with respect to the unknown parameters. Only a simple MATLAB® program needs to be run for the identification. Since there is no need to compute statically admissible stress fields at each time step, but the strains are used to obtain stresses using some initial material parameters and then equilibrium checked directly on these. This method is computationally efficient. In a previous study, the VFM was extended to characterize the material behavior under tension-compression (Pierron et al., 2010a), with reasonable NLKH parameters identified. This however, was limited to only one reverse loading path since the specimens buckled at an early stage during compression.

The present work is aimed at developing a method to characterize the material behavior of AHSS subjected to a few reverse loading cycles. To study this, the NLKH models combined with Voce type isotropic hardening are selected to describe the material behavior. The cases of multi-backstress components are considered. The VFM is applied to identify the material constitutive parameters. First, in Section 2, the formulations of the NLKH and the identification procedure are introduced. Then, in Section 3, the proposed identification method is validated on FE simulations of forward-reverse simple shear. In Section 4, the validated method is applied to the selected AHSS, namely, dual-phase (DP600), transformation-induced plasticity (TRIP780) and twinning-induced plasticity (TWIP980) steels, subjected to two cycles of forward-reverse simple shear, to identify their constitutive parameters.

2. Methodology

2.1. Nonlinear kinematic hardening

The NLKH models considered in this study are based on the von Mises yield criterion and a kinematic hardening rule. For a yield condition:

$$\mathcal{F} = f(\boldsymbol{\sigma} - \boldsymbol{\alpha}) - \sigma_s(\varepsilon_p) = 0 \tag{1}$$

$f(\boldsymbol{\sigma} - \boldsymbol{\alpha})$ is the equivalent stress with respect to the stress tensor $\boldsymbol{\sigma}$ and the backstress tensor $\boldsymbol{\alpha}$, while σ_s is the current yield stress under the equivalent plastic strain ε_p. The equivalent stress is defined as:

$$f(\boldsymbol{\sigma} - \boldsymbol{\alpha}) = \sqrt{\frac{3}{2}\left(\boldsymbol{s} - \boldsymbol{\alpha}^{dev}\right) : \left(\boldsymbol{s} - \boldsymbol{\alpha}^{dev}\right)} \tag{2}$$

where $\boldsymbol{s}$ is the deviatoric stress tensor and $\boldsymbol{\alpha}^{dev}$ the deviatoric backstress tensor. ":" stands for the tensor inner product. For NLKH, the yield surface not only translates in stress space through the backstress tensor $\boldsymbol{\alpha}$ but also expands istropically following the evolution of the current yield stress σ_s. The NLKH term was initially proposed by Armstrong and Frederick (1966), Frederick and Armstrong (2007) (denoted A-F model) in the form:

$$\mathrm{d}\boldsymbol{\alpha} = \frac{C}{\sigma_s}(\boldsymbol{\sigma} - \boldsymbol{\alpha})d\varepsilon_p - \gamma\boldsymbol{\alpha}d\varepsilon_p \tag{3}$$

where C is the kinematic hardening modulus, and γ is the parameter that determines the decrease of kinematic hardening. Later, the range of validity of this model was widened by Chaboche (1986) (denoted CNLKH model) after superimposing several models of the same type in the following form:

$$\mathrm{d}\boldsymbol{\alpha}_i = \frac{C_i}{\sigma_s}(\boldsymbol{\sigma} - \boldsymbol{\alpha})d\varepsilon_p - \gamma_i\boldsymbol{\alpha}_i d\varepsilon_p \tag{4}$$

and the overall backstress tensor

$$\boldsymbol{\alpha} = \sum_{i=1}^{N}\boldsymbol{\alpha}_i \tag{5}$$

where N is the number of components of the backstress tensor. It should be mentioned that the above CNLKH model (Eq. (4)) is expressed in a different form than the equation in Chaboche (1986) in order to be consistent with the commercial finite element code, ABAQUS.

For the evolution of the yield surface size, Voce hardening is considered in this study, and thus,

$$\sigma_s(\varepsilon_p) = Y_0 + R_{sat}\left(1 - e^{-n\varepsilon_p}\right) \tag{6}$$

where Y_0 stands for the initial yield stress, R_{sat} the saturation stress, and n the material constant that defines the change rate of the yield surface size. In order to predict the Bauschinger effect of a material subjected to cyclic loads using FE simulation, the material constitutive parameters (Y_0, R_{sat}, n, C_i and γ_i) must be determined first. In the present study, this inverse problem is solved using the VFM.

2.2. The virtual fields method

The VFM utilizes the equilibrium equations deduced from the principle of virtual work. For a given solid object of volume V, which is subjected to a quasi-static loading vector $\boldsymbol{T}$ acting on the

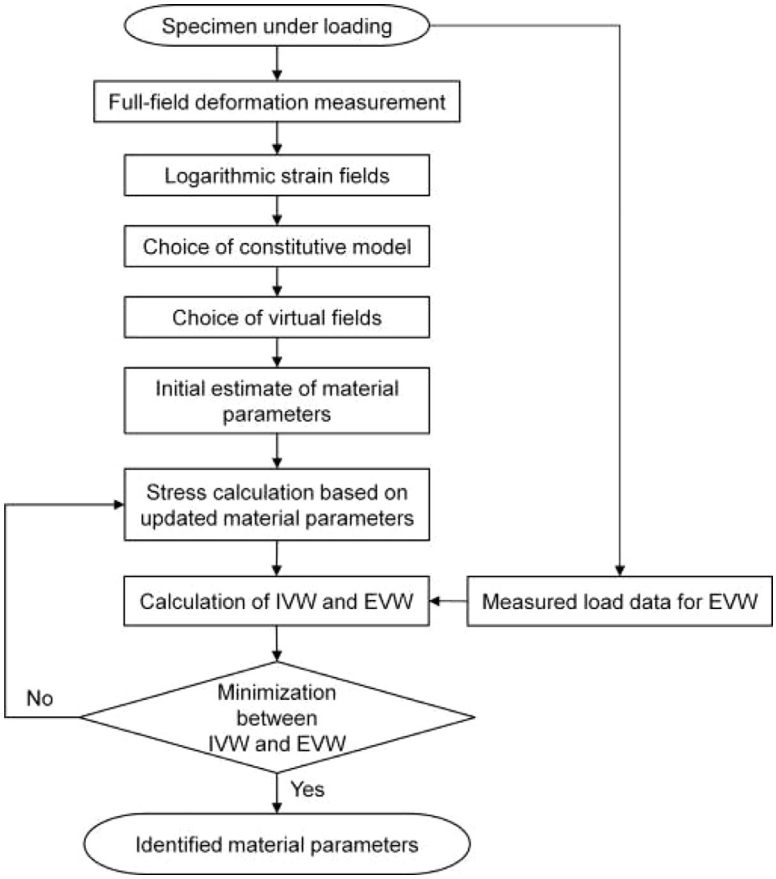

Fig. 1. Flow chart of the inverse scheme for parameter identification.

object boundary ∂V, if the body force is negligible, this principle can be written as:

$$\underbrace{-\int_V \boldsymbol{\sigma} : \boldsymbol{\varepsilon}^*\, dV}_{\text{Internal virtual work}} + \underbrace{\int_{\partial V} \boldsymbol{T}.\boldsymbol{u}^*\, dS}_{\text{External virtual work}} = 0 \tag{7}$$

where $\boldsymbol{u}^*$ is the virtual displacement vector and $\boldsymbol{\varepsilon}^*$ the corresponding virtual strain tensor derived from $\boldsymbol{u}^*$. In Eq. (7), the first term in the left hand side is denoted as internal virtual work (IVW) while the second term as external virtual work (EVW). Essentially, a selected virtual displacement field $\boldsymbol{u}^*$ is a test function that produces a particular integral equilibrium equation. The virtual displacement field must be continuous and differentiable across the whole volume. There are infinite choices for virtual fields. However, in practice, the selected virtual fields should have null values over the fixed boundaries where the reaction forces are difficult to measure. This is to cancel out the EVW contributed by the unknown reaction forces. For the moving boundaries, the selected virtual fields should be constant in the loading direction, but zero in the transverse one so that the equilibrium Eq. (7) contains the measured resulting load. In the case of elasto-plasticity, the equilibrium equation is written as:

$$-\int_V \int_0^t \dot{\sigma}\, dt : \varepsilon^*\, dV + \int_{\partial V} \boldsymbol{T}.\boldsymbol{u}^*\, dS = 0 \tag{8}$$

where $\dot{\boldsymbol{\sigma}} = \frac{d\boldsymbol{\sigma}}{dt}$ is the stress rate tensor, and the stress tensor at time t is calculated from $\int_0^t \dot{\boldsymbol{\sigma}}\, dt$. It is worth noting that stress is not directly measurable in practice whereas strain can be measured by various deformation measurement techniques. It is hence necessary to determine the relationship between the stress and strain increments so that the stress values can be calculated. Here, the radial return stress calculation algorithm developed by Sutton et al. (1996) is adopted, which is based on the decomposition of elastic and plastic strain increments, the associated flow rule, and the consistency condition, as detailed in Appendix A. Based on this algorithm, the stress increment vector $d\boldsymbol{\sigma}$ can be expressed by the total strain increment vector $d\boldsymbol{\varepsilon}$ through the relation:

$$d\boldsymbol{\sigma} = \left(\mathbf{Q} - \frac{\mathbf{Q} : \frac{\partial \mathcal{F}}{\partial \boldsymbol{\sigma}} \otimes \mathbf{Q} : \frac{\partial \mathcal{F}}{\partial \boldsymbol{\sigma}}}{\frac{\partial \mathcal{F}}{\partial \boldsymbol{\sigma}} : \mathbf{Q} : \frac{\partial \mathcal{F}}{\partial \boldsymbol{\sigma}} - \frac{\partial \mathcal{F}}{\partial \varepsilon_p}} \right) : d\boldsymbol{\varepsilon} \tag{9}$$

where $\mathbf{Q}$ stands for the elastic stiffness matrix, and $\mathcal{F}$ is the yield condition denoted in Eq. (1). Since $d\boldsymbol{\sigma}$ is a nonlinear function of $d\boldsymbol{\varepsilon}$ with respect to the actual stress $\boldsymbol{\sigma}$, the equivalent plastic strain ε_p, and the unknown constitutive parameters, the identification procedure thus is iterative in nature. This is implemented by establishing a cost function that measures the gap between the IVW and the EVW and minimizing it with respect to the unknown parameters (denoted $\boldsymbol{X}$). For the sheet specimen with thickness b considered in the present study, this cost function writes:

$$\mathcal{C}(\boldsymbol{X}) = \sum_{j=1}^{N_j} \left(-b \int_A \left(\int_0^t \dot{\sigma}\, dt \right) : \boldsymbol{\varepsilon}^* dS + \int_{\partial V} T.u^*\, dS \right)^2 \tag{10}$$

where N_j is the total number of loading increments, and A is the area of interest (AOI). The above inverse scheme has been implemented by the authors in MATLAB® programming environment, which follows the procedure illustrated in the flow chart in Fig. 1. When performing identification, the measured full-field strain data and the load data are imported into the MATLAB® program. Based on the selected constitutive model and the virtual fields, the strain data are utilized to compute the IVW and the load data for the EVW using Eqs. (9) and (10). An initial estimate of the

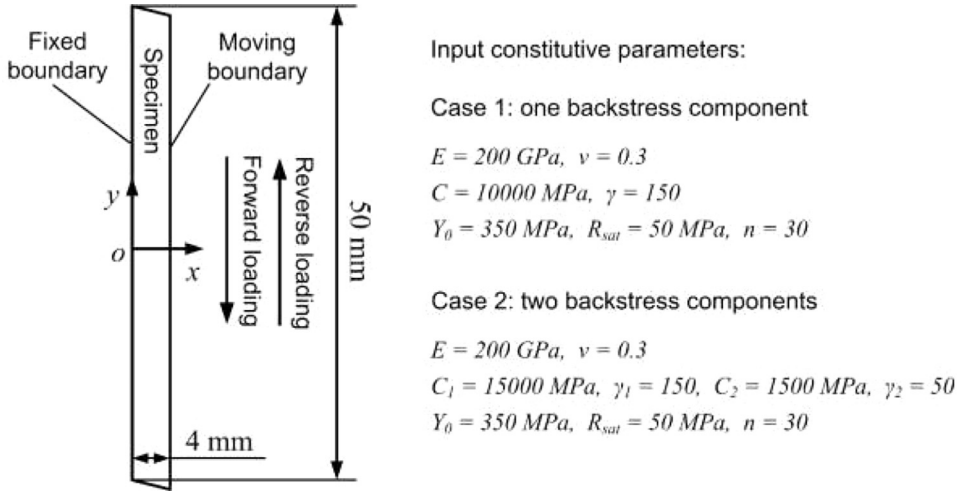

Fig. 2. FE model of the forward-reverse simple shear.

material parameters needs to be selected to start the minimization process, which is updated iteratively until the convergence is reached. The nonlinear least-square algorithm ('lsqnonlin' algorithm in MATLAB®) is used to minimize the cost function $C(\boldsymbol{X})$, which calculates the quadratic gap between the IVW and the EVW. Finally, the identified material parameters can be obtained.

3. Numerical verification

3.1. FE simulations

In order to examine the effectiveness of the proposed identification method, FE models that simulate the forward-reverse simple shear were developed using ABAQUS® as shown in Fig. 2. The advantage of this deformation configuration is that it allows the specimen to experience high strain level without buckling, which, however, is a limitation for sheet tension-compression as buckling usually occurs at an early stage of compression. The simulated strain and load data were exported from ABAQUS® and utilized in the proposed VFM scheme for parameter identification. The idea is to check if the identified parameters match with the reference values that are input in the FE simulations so that the identification accuracy can be evaluated. Fig. 2 shows the schematic of the forward-reverse simple shear, for both of the FE simulations and the experiments considered in the present study. The left boundary of the rectangular specimen is fixed while the right boundary is driven in a forward-reverse manner. For the FE simulations, a 2D shell model was selected with the shell thickness of 1 mm. The element type is triangular, and with a global mesh size of 0.5 mm. Two cases have been studied for the FE simulations based on the NLKH. In the first case, only one backstress component was considered (A-F model) while in the second case, two backstress components were considered (CNLKH model). The input constitutive parameters were somehow arbitrarily chosen for the two cases and are given in Fig. 2, which are reasonable values for this type of parameters (Broggiato et al., 2008; Rezaiee-Pajand and Sinaie, 2009). Displacements along the *y*-direction were applied to the right boundary in a cyclic manner. One forward loading path together with the subsequent reverse one is counted as one loading cycle (i.e. LP1 + LP2). At least one loading cycle is necessary for parameter identification since the kinematic hardening behavior cannot be separated from the isotropic hardening behavior until a load reversal occurs. Here, different numbers of loading cycles, as listed in Table 1, have been studied to investigate their influence on the identification results. A displacement of 0.2 mm was applied for each loading path,

Table 1
Three loading histories of the simulated forward-reverse simple shear (unit: mm, LP: loading path, LH: loading history).

	LP1	LP2	LP3	LP4
LH 1	0.2	-0.2	/	/
LH 2	0.2	-0.2	0.2	/
LH 3	0.2	-0.2	0.2	-0.2

Table 2
Identification results obtained with simulation data for the case of one backstress component (LH: loading history).

	C (MPa)	γ	Y_0 (MPa)	R_{sat} (MPa)	n
Reference values	10,000	150	350	50	30
Initial estimate 1	5000	50	200	20	20
LH 1	9735	146	350	49.9	30.8
LH 2 Identified	9765	147	350	50.3	29.9
LH 3	9783	147	350	50.0	30.3
Initial estimate 2	20,000	500	500	50	50
LH 1	9735	146	350	49.9	30.8
LH 2 Identified	9765	147	350	50.3	29.9
LH 3	9783	147	350	50.0	30.3

and each loading path was comprised of 100 loading increments. For each loading increment, the logarithmic strain at the centroid of each element and the load at each node of the right boundary were exported from ABAQUS® for parameter identification.

For the VFM, several virtual fields have been attempted, which have zero value on the fixed boundary and constant value on the moving boundary, as explained in Section 2.2. Since no significant difference was observed in the identification results, the simplest virtual field, denoted as VF1, is kept in the present work.

$$VF1: \; u_x^* = 0, \; u_y^* = x \Rightarrow \varepsilon_{xx}^* = 0, \; \varepsilon_{yy}^* = 0, \; \varepsilon_{xy}^* = 0.5 \tag{11}$$

where u_x^* and u_y^* are the virtual displacements along *x*- and *y*-direction, respectively, ε_{xx}^*, ε_{yy}^*, and ε_{xy}^* are the deduced virtual strains, and *x* is the horizontal coordinate of each element center.

3.2. Identification results for the FE simulations

3.2.1. One backstress component

The identification results obtained with different loading histories are reported in Table 2. In order to investigate the robustness of the VFM algorithm in providing a globally optimized solution, two different initial estimates were arbitrarily chosen to start the

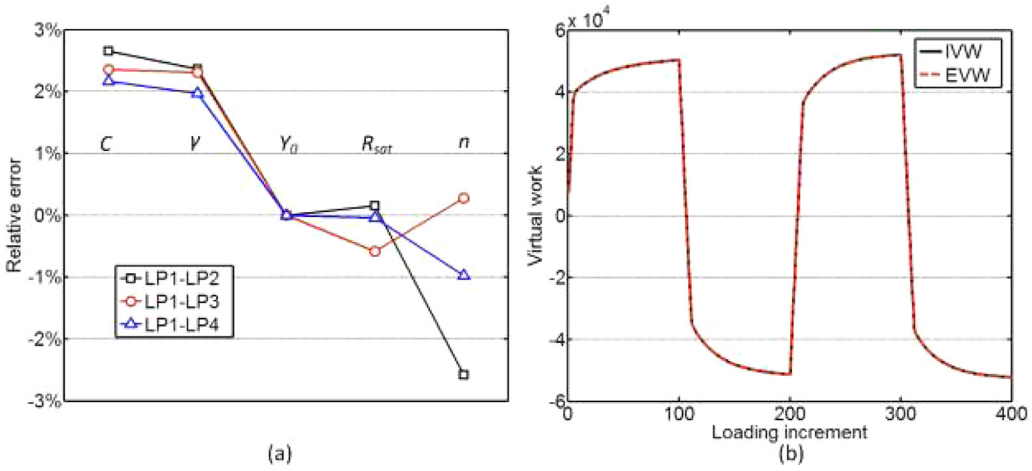

Fig. 3. (a) Relative errors of identified constitutive parameters, and (b) Plot of internal virtual work and external virtual work (Initial estimate 1, LH 3) for the case of one backstress component.

Table 3
Identification results obtained with simulation data for the case of two backstress components.

	C_1 (MPa)	γ_1	C_2 (MPa)	γ_2	Y_0 (MPa)	R_{sat} (MPa)	n
Reference values	15,000	150	1500	50	350	50	30
Initial estimate 1	10,000	100	1000	10	200	20	20
LH 1	14,275	151	1951	55.5	350	50.3	30.7
LH 2 Identified	14,756	145	1349	47.5	350	50.2	30.2
LH 3	14,618	148	1563	50.7	350	50.1	30.4
Initial estimate 2	20,000	200	2000	100	500	100	50
LH 1	14,276	151	1951	55.5	350	50.3	30.7
LH 2 Identified	14,756	145	1349	47.5	350	50.2	30.2
LH 3	14,618	148	1563	50.7	350	50.1	30.4

minimization process. As can be seen in Table 2, for the two sets of initial values, the identification results are identical for the same loading histories, indicating that this minimization algorithm is not hampered by local minima when starting from different initial estimates having reasonable orders of magnitude. For loading history 1 (LP1 – LP2), which is the case of only one loading cycle, the identified parameters are in good agreement with the reference values. The relative errors of identified parameters are plotted in Fig. 3a, which shows that the error level is just a few percent. For loading histories 2 (LP1 – LP3) and 3 (LP1 – LP4), when more loading cycles are included, the identification accuracy is slightly improved, as can be observed in Table 2 and Fig. 3a. In Fig. 3b, the IVW and the EVW are plotted for each loading increment of the whole deformation process (loading history 3) when the minimization algorithm (started from initial estimate 1) reached the convergence. Evidently, the two curves exhibit very close agreement, and thus verify the reliability of the identification results. Overall, for the NLKH model with one backstress component, one loading cycle is sufficient to provide a stable parameter identification. However, involving more loading cycles is expected to provide a more comprehensive characterization of material behavior. An advantage of this identification method is the efficiency of convergence, which only takes around three minutes for all cases.

3.2.2. Two backstress components

The identification results for the case of two backstress components are given in Table 3, and the relative errors of the seven identified parameters are plotted in Fig. 4a. Similar to the previous case, identical identification results were obtained from the different initial estimates, indicating that local minimization is not an issue here. It can be noted that, for all loading histories, the identified Voce hardening parameters are in good agreement with their reference counterparts. However, the NLKH parameters are determined accurately only when the loading cycles are no less than two, particularly for C_2 and γ_2. The explanation for this is that a certain number of load reversals are needed to separate the contribution of each backstress component to the kinematic hardening behavior. As for the case of one backstress component, the IVW and the EVW are plotted in Fig. 4b for the initial estimate 1 and loading history 3. Again, good agreement can be found between the two curves so that the reliability of the identification results is verified. Based on the above observations, loading history 3 provides the best identification results at a minimum cost and is kept for the experimental applications in this study.

3.3. Influence of noise

To have a general idea of the influence of noise in strain measurement on the identification accuracy, random Gaussian white noise was added to the simulated strain data for the whole deformation process (LP1-LP4). The noise amplitudes of 1.92×10^{-4}, 1.72×10^{-4}, and 1.42×10^{-4} for ε_{xx}, ε_{yy}, and ε_{xy}, respectively, were selected according to the noise level of the strain measurements obtained experimentally in the present work. The experimental procedure of strain measurement will be introduced in the next section. The noise-polluted strain data were then input into the VFM program for parameter identification, and the results are given in Tables 4 and 5 for the cases of one and two backstress components, respectively. As expected, for both cases, compared to the identification results without noise in Tables 2 and 3, the global error level is a bit increased after adding noise. The shear stress-strain curves calculated using the identified parameters with and without noise effect are compared with the reference curves in Fig. 5. It can be observed that, for both cases, when noise is not added, the identified curves precisely match with the reference curves. After adding noise, the identified curves are still in

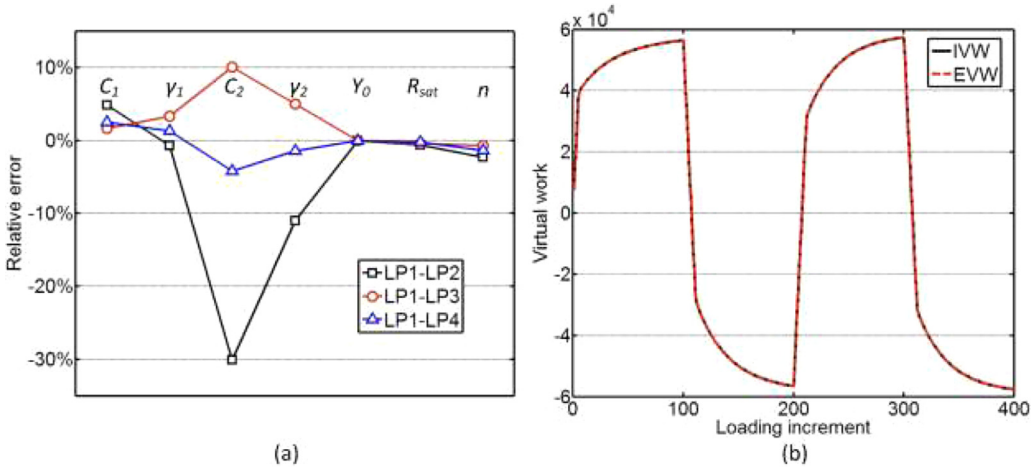

Fig. 4. (a) Relative errors of identified constitutive parameters, and (b) Plot of internal virtual work and external virtual work (Initial estimate 1, LH 3) for the case of two backstress components.

Table 4
Identification results obtained with noise-polluted strain data for the case of one backstress component (LH 3: LP1-LP4).

	C (MPa)	γ	Y_0 (MPa)	R_{sat} (MPa)	n
Reference values	10,000	150	350	50	30
Initial estimate 1	5000	50	200	20	20
Identified 1	10,552	155	357	49.4	33.6
Relative error (%)	5.52	3.33	2.08	−1.12	11.9
Initial estimate 2	20,000	500	500	50	50
Identified 2	10,552	155	357	49.4	33.6
Relative error (%)	5.52	3.33	2.08	−1.12	11.9

good overall agreement with the reference curves, although slight deviations can be observed, corresponding to the increased identification errors in Tables 4 and 5. An approach based on the choice of optimal virtual fields as introduced by Pierron et al. (2010a) can reduce the effect of noise and thus may improve the identification accuracy. However, at this stage, these results are satisfactory and suggest that this identification method is suitable for identifying material parameters from real experiments.

4. Experimental applications

4.1. Materials and experiments

Three types of AHSS have been considered in this study, which are DP600, TRIP780 and TWIP980. For all materials, the specimens were cut from bigger sheets to a shape of 50×4 mm, with 1.42, 1.43 and 1.25 mm thickness for the DP600, TRIP780 and TWIP980, respectively. The specimens were tested under forward-reverse simple shear. It should be mentioned that the experiments were previously performed for parameter identification of the homogeneous anisotropic hardening (HAH) model (Barlat et al., 2011). A detailed description of the experiments has been provided elsewhere (Fu et al., 2016). In the present work, these experimental measurements were reused for the calibration of the NLKH models. Thus, only a brief introduction of the experimental procedure is given here.

The specimens were tested in the simple shear experimental set-up (Choi et al., 2015) in a way as illustrated in Fig. 2. The experimental set-up and a speckle pattern image are illustrated in Fig. 6. Two loading cycles were conducted for each specimen as suggested in Section 3. A mode of displacement control was chosen for the tests with a low cross-head speed of 0.01 mm s^{-1}, which corresponds to a strain rate of about 1.25×10^{-3} s^{-1}. The strain level for each loading path is around 5%, which, however, differs for the selected steels due to the compliance of the test device with respect to the different material strengths. For each material, two tests were performed in order to check the repeatability of the results.

During the tests, the full-field deformations were measured using a stereo digital image correlation (SDIC) system. First, a series of stationary speckle images (2048×2448 pixels along the x and y directions, respectively) of a specimen were recorded and deformation analysis was performed using DIC. The noise level of strain measurement was determined by calculating the standard deviations of the strain values by taking ten images of speckle pattern at rest. When performing DIC in the commercial DIC software VIC-3D, a subset size of 33×33 pixels with a step size of 11 pixels was chosen. For the strain components ε_{xx}, ε_{yy}, and ε_{xy}, the strain noise levels were 1.92×10^{-4}, 1.72×10^{-4}, and 1.42×10^{-4}, respectively. Then, for each specimen, a reference image was taken before deformation, and the images during deformation were taken at a frequency of one image per second. Synchronized load data

Table 5
Identification results obtained with noise-polluted strain data for the case of two backstress components (LH 3: LP1-LP4).

	C_1 (MPa)	γ_1	C_2 (MPa)	γ_2	Y_0 (MPa)	R_{sat} (MPa)	n
Reference values	15,000	150	1500	50	350	50	30
Initial estimate 1	10,000	100	1000	10	200	20	20
Identified 1	16,136	156	1551	52.6	357	48.9	33.9
Relative error (%)	7.57	3.67	3.43	5.24	4.11	−2.12	13.0
Initial estimate 2	20,000	200	2000	100	500	100	50
Identified 2	16,136	156	1551	52.6	357	48.9	33.9
Relative error (%)	7.57	3.67	3.43	5.24	4.11	−2.12	13.0

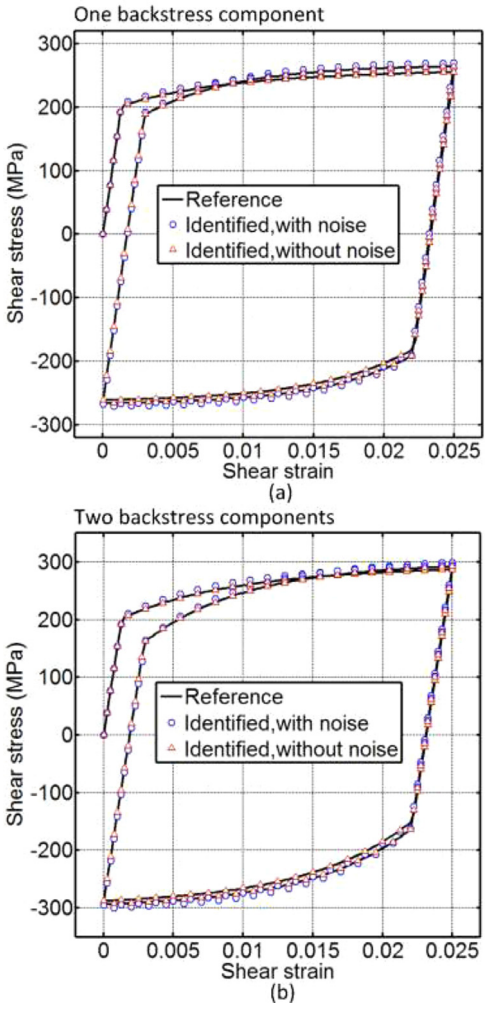

Fig. 5. Shear stress-strain curves calculated by the identified parameters with and without noise effect considered v.s. the reference curves, (a) one backstress component and (b) two backstress components (using Identified 1, LH3 in Table 2 to Table 5).

were recorded by a load cell. Note that, for the sake of a good spatial resolution, only the central region of the specimen (4×20 mm along the x and y directions, respectively) was used for the area of interest (AOI). In Fig. 7, the logarithmic shear strain fields, measured by DIC, at different loading stages are shown. It can be seen that there are strain concentrations on both left and right boundaries. These were induced by the serrated groove of the grips which was designed to prevent the specimen from slipping during deformation. For parameter identification using the VFM, the logarithmic strains were calculated using an analytical procedure and the finite deformation theory as explained in Avril et al. (2010), Kim et al. (2013). A brief introduction regarding this is given in Appendix B.

4.2. Identification results for the AHSS

Once the strain and load data were obtained, they were processed with the VFM as explained in previous sections. The virtual field VF1 in Eq. (11) was selected. For each material, the results are presented here only for one specimen since no significant difference was observed between the two specimens. It should be mentioned that Young's modulus E and Poisson's ratio ν are necessary for the determination of the stiffness matrix $\boldsymbol{Q}$ in Eq. (9). E was

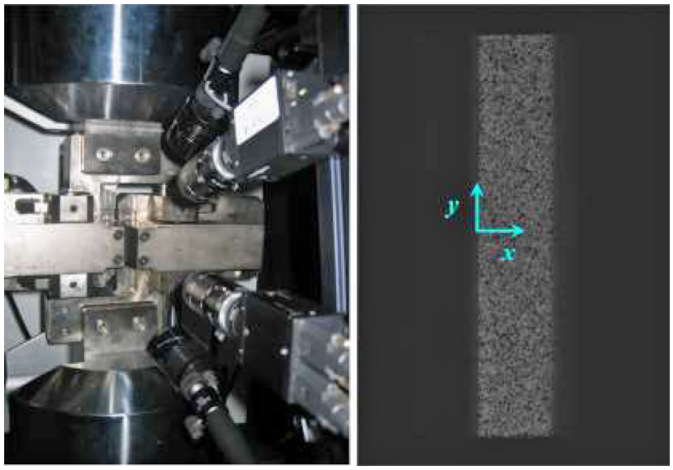

Fig. 6. Experimental set-up and a speckle pattern image.

derived from ν and shear modulus G through the relation:

$$E = 2G(1+\nu) \tag{12}$$

where G was calculated from the slope of the experimental shear stress-strain curve in the initial linear range, and ν was set to a reasonable approximation of 0.3 according to (Chung et al., 2011; Kim et al., 2013). Reasonable Young's moduli were obtained for the DP600, TRIP780 and TWIP980, which are 212, 209 and 192 GPa, respectively.

4.2.1. DP600

As suggested in Section 3.2.1, one loading cycle is sufficient to provide a reasonable parameter identification for the case of one backstress component. Nevertheless, for the experimental data, it is interesting to compare the identified parameters obtained with one loading cycle to those obtained with more loading cycles. In Table 6, the identification results based on one cycle and two cycles are given for the DP600. It can be observed that although the identified parameters obtained with the two loading histories are not identical, the difference is insignificant. One way to check this difference is to fix the constitutive parameters in the cost function using the results obtained with one loading cycle and then calculate the cost function value (CFV) for two loading cycles, here, 8.89×10^7, as given in Table 6. This value is very close to the CFV of the 2-loading cycle identification. The latter, namely 7.34×10^7, is slightly smaller, indicating that the fitting between IVW and EVW is slightly better. This is expected since the identification in the latter case is based on a more comprehensive loading history. It should be mentioned that two different initial estimates have been attempted for each case, and the identification results are almost identical, as can be seen in Table 6. In Fig. 8a, the shear stress-shear strain curves (green dash dot line for the case of one loading cycle and black dot line for the case of two loading cycles, one backstress component) calculated using the identified parameters (Identified 1) are compared with their experimental counterpart. For the experimental counterpart, the shear stress σ_{xy} was given by the ratio between the measured load and the cross sectional area along the y-direction, and the shear strain ε_{xy} was given by the mean shear strain value in the AOI measured with DIC. In Fig. 8b, the identified curves and the experimental counterpart are plotted with respect to the cumulated shear strain and the absolute values of shear stress for the sake of legibility. One can see that both identified curves are reasonably consistent with the experimental curve although discrepancies can be found towards the end of each loading path. This is not surprising since the NLKH model with only one backstress component is probably not

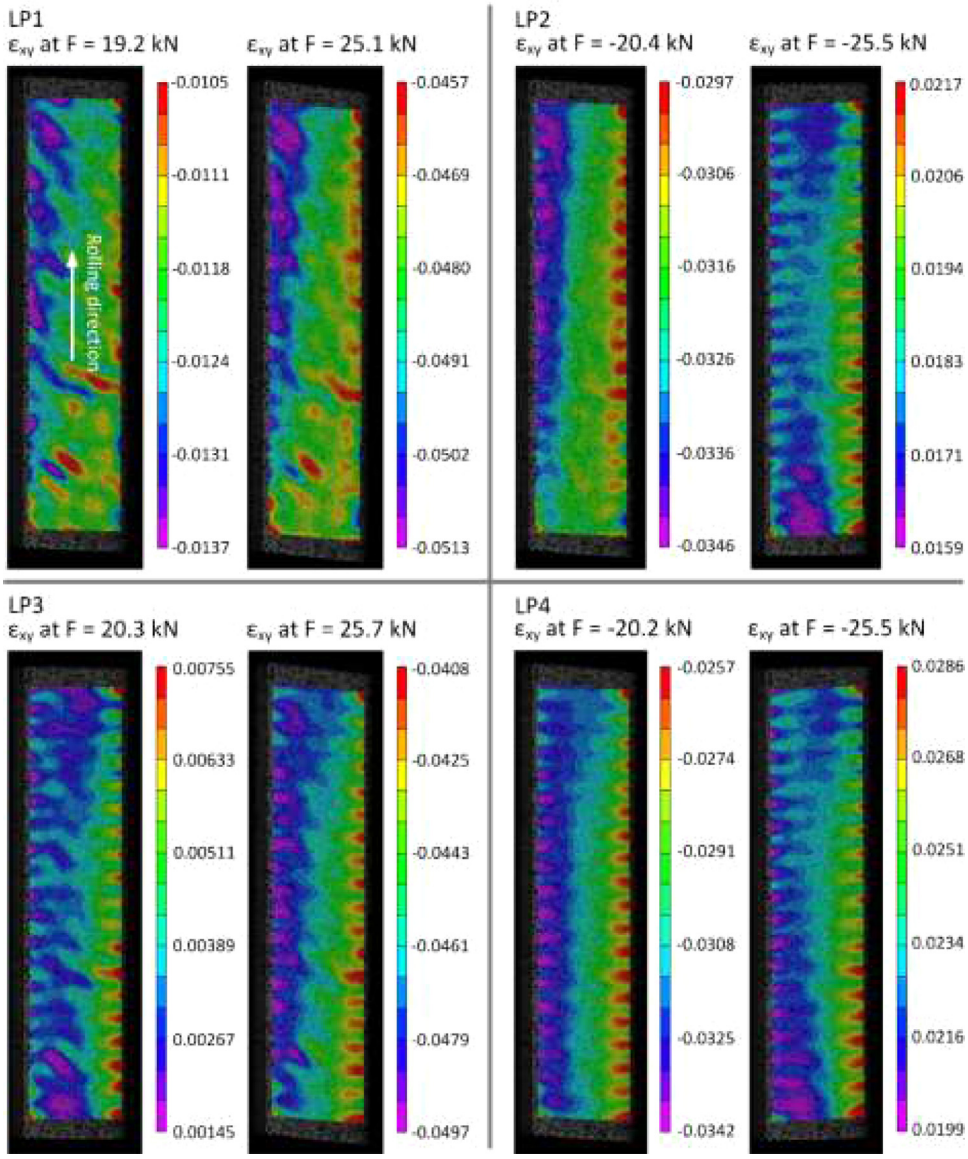

Fig. 7. Logarithmic shear strain fields at different loading stages measured with DIC.

Table 6
Identification results for the DP600 for the case of one backstress component (CFV: cost function value).

	C (MPa)	γ	Y_0 (MPa)	R_{sat} (MPa)	n	CFV	
Initial estimate 1	10,000	100	100	10	10		1 cycle
Identified 1	24,406	110	295	78.4	28.8	8.89×10^7	
Initial estimate 2	50,000	500	500	100	100		
Identified 2	24,407	110	295	78.4	28.8	8.89×10^7	
Initial estimate 1	10,000	100	100	10	10		2 cycles
Identified 1	28,895	121	281	70.5	34.1	7.34×10^7	
Initial estimate 2	50,000	500	500	100	100		
Identified 2	28,896	121	281	70.5	34.1	7.34×10^7	

sufficient to describe the material behavior thoroughly. One can also observe that the difference between the two identified curves is insignificant, which was expected. For other materials in the following sections, only the identification results obtained with two loading cycles will be given considering the smaller CFV.

For the NLKH model with two backstress components, the identification results are given in Table 7. Similar to the previous cases, two initial estimates were selected to start the minimization. Again, the identified parameters obtained with different initial estimates were in good agreement with each other, confirming the robustness of the proposed VFM scheme. Interestingly, when one more backstress component is added, the CFV is significantly reduced from 7.34×10^7 to 3.11×10^7, indicating a better match between the IVW and the EVW. In Fig. 8, the shear stress-shear strain curve based on these parameters (Identified 1) is plotted. One can clearly see that the fitting between this curve and the experimental counterpart is substantially improved compared to the case of the curves for one backstress component, with the

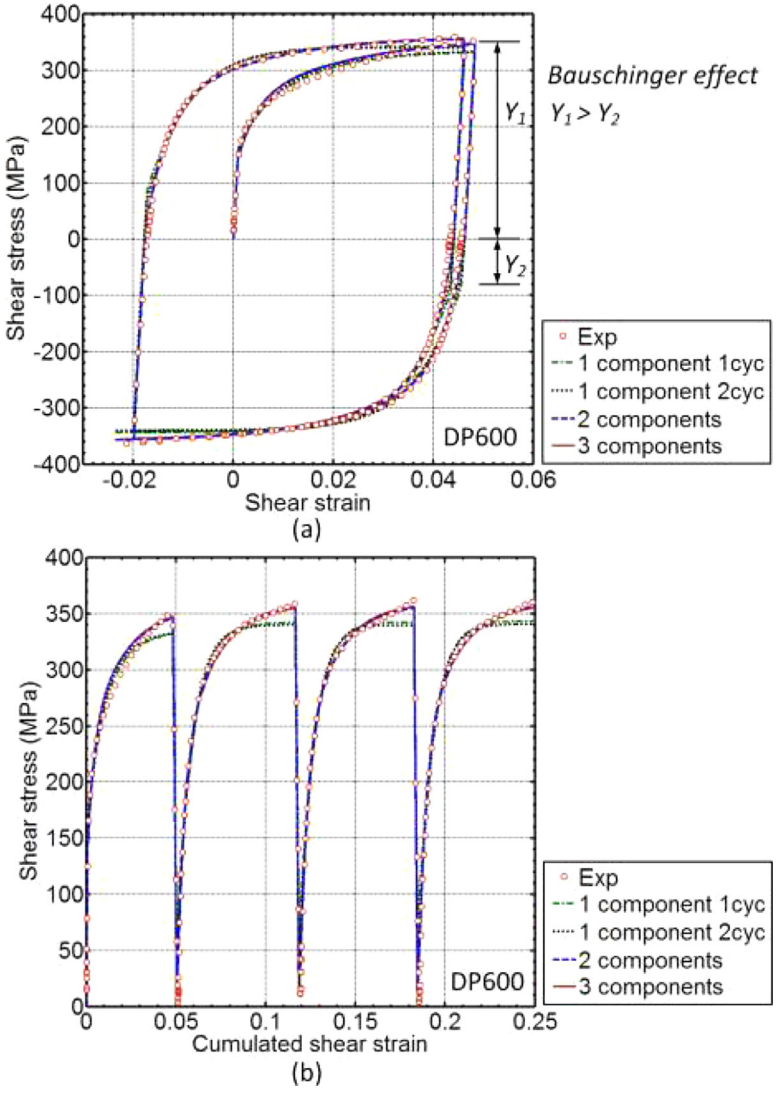

Fig. 8. Experimental and identified shear stress-strain curves for the DP600 in forward-reverse simple shear obtained with Identified 1, plotted with respect to (a) true strain (b) cumulated strain.

Table 7
Identification results for the DP600 for the case of two backstress components (two loading cycles).

	C_1 (MPa)	γ_1	C_2 (MPa)	γ_2	Y_0 (MPa)	R_{sat} (MPa)	n	CFV
Initial estimate 1	20,000	200	2000	20	200	50	10	
Identified 1	48,874	283	6221	49.3	246	79.7	33.7	3.11×10^7
Initial estimate 2	80,000	500	8000	100	500	100	50	
Identified 2	48,701	282	6142	48.9	246	79.8	33.7	3.12×10^7

discrepancies observed towards the end of each loading path significantly reduced. The reason for this is that two backstress components provide better fit to describe the material behavior than only one component. This is consistent with the observation in Chaboche (1986) that the hysteresis curve representation gradually improves with more backstress components. In order to further study the influence of multicomponents, the Chaboche model with three components (two nonlinear components plus one linear component, in which γ_3 equals zero) has been applied. The identification results are given in Table 8. One can see from the cost function values that three components only provide a marginally better fit. The shear stress-shear strain curves for the three-component and the two-component cases in Fig. 8 almost overlap with each other. Nevertheless, the improvement of three components is expected to be more significant when material is subjected to more loading cycles. In other words, adding even more components in the model is expected to further improve the fitting, which, however, will require more loading cycles to guarantee a reasonable identification as discussed in Section 3.2.2 and will also increase the possibility of local minima.

It is worth noting that from the experimental curves, the Bauschinger effect can be clearly observed by comparing the reloading yield stress to the previous yield stress before load reversal, e.g., the significant drop from Y_1 to Y_2 in Fig. 8a. The identified curves suggest that the NLKH models are able to capture this effect.

Table 8
Identification results for the DP600 for the case of three backstress components (two loading cycles).

	C_1 (MPa)	γ_1	C_2 (MPa)	γ_2	C_3 (MPa)	Y_0 (MPa)	R_{sat} (MPa)	n	CFV
Initial estimate 1	20,000	200	2000	20	200	200	50	10	
Identified 1	48,704	286	6399	52.5	135	246	81.3	33.7	3.04×10^7
Initial estimate 2	80,000	500	8000	100	500	500	100	50	
Identified 2	48,308	283	6272	51.9	134	246	81.5	33.7	3.04×10^7

Table 9
Identification results for the TRIP780 for the case of one backstress component (two loading cycles).

	C (MPa)	γ	Y_0 (MPa)	R_{sat} (MPa)	n	CFV
Initial estimate 1	10,000	100	100	10	10	
Identified 1	38,111	124	344	90.5	14.4	2.14×10^8
Initial estimate 2	50,000	500	500	100	100	
Identified 2	38,088	124	344	90.6	14.4	2.14×10^8

Table 10
Identification results for the TRIP780 for the case of two backstress components (two loading cycles).

	C_1 (MPa)	γ_1	C_2 (MPa)	γ_2	Y_0 (MPa)	R_{sat} (MPa)	n	CFV
Initial estimate 1	20,000	200	2000	20	200	50	10	
Identified 1	55,540	371	17,117	79.1	306	96.1	15.4	1.68×10^8
Initial estimate 2	80,000	500	8000	100	500	100	50	
Identified 2	58,085	380	16,998	78.1	304	96.8	15.1	1.69×10^8

Table 11
Identification results for the TRIP780 for the case of three backstress components (two loading cycles).

	C_1 (MPa)	γ_1	C_2 (MPa)	γ_2	C_3 (MPa)	Y_0 (MPa)	R_{sat} (MPa)	n	CFV
Initial estimate 1	20,000	200	2000	20	200	200	50	10	
Identified 1	55,478	376	17,641	80.4	5.77	305	96.2	15.1	1.68×10^8
Initial estimate 2	50,000	500	5000	100	100	500	100	50	
Identified 2	55,624	355	16,169	76.8	7.18	305	97.3	15.1	1.69×10^8

Table 12
Identification results for the TWIP980 for the case of one backstress component (two loading cycles).

	C (MPa)	γ	Y_0 (MPa)	R_{sat} (MPa)	n	CFV
Initial estimate 1	10,000	100	100	10	10	
Identified 1	34,481	75.2	521	47.6	2462	6.62×10^8
Initial estimate 2	50,000	500	500	100	100	
Identified 2	34,959	76.6	566	1.00×10^{-5}	16,302	6.61×10^8

4.2.2. TRIP780

The identified parameters for the TRIP780 are given in Tables 9–11 for the cases of one, two, and three backstress components, respectively. As can be seen, the identification results are consistent with each other when started from different initial estimates. The models with two and three components provide very close CFV, both smaller than the case of one component. The shear stress-shear strain curves calculated using the identified parameters (Identified 1) are given in Fig. 9 and compared with their experimental counterpart. One can see that the identified curves are generally in good agreement with the experimental curve, with Bauschinger effect properly captured, although the match is not as good compared to that of the DP600 in Fig. 8. Expected from the smaller CFV, the models with two and three components provide a slightly better match with the experimental curve.

4.2.3. TWIP980

For the TWIP980, the identification results based on one backstress component are given in Table 12. Interestingly, with different initial estimates, the results are significantly different for the Voce hardening parameters, particularly for the parameters R_{sat} and n. One can see that n tends to be a very high value, which makes the term $R_{sat}(1-e^{-n\varepsilon_p})$ in Eq. (6) close to zero. In this case, the current yield stress σ_s becomes a constant Y_0, which indicates that the yield surface translates in stress space but its shape is maintained. One question that arises is whether or not the constant current yield stress is due to the use of Voce hardening since the Voce hardening tends to saturate quickly. To answer this question, another two isotropic hardening laws were used to substitute the Voce hardening and combined with the NLKH model (one backstress component), namely, the Swift and the Modified Voce hardening laws, which write:

$$Swift\ hardening:\ \sigma_s(\varepsilon_p) = Y_{0S}(\varepsilon_{0S}+\varepsilon_p)^{n_s} \tag{13}$$

$$Modified\ Voce\ hardening:\ \sigma_s(\varepsilon_p) = Y_{0M} + R_{0M}\varepsilon_p + R_{satM}\left(1-e^{-n_M\varepsilon_p}\right) \tag{14}$$

where Y_{0S}, ε_{0S}, n_s are the Swift hardening parameters, and Y_{0M}, R_{0M}, R_{satM}, n_M are the modified Voce hardening parameters. The identification results based on these are given in Table 13. It clearly shows that even different isotropic hardening laws are adopted, the current yield stress $\sigma_s(\varepsilon_p)$ still exhibits approximately a constant value, Y_{0S} for the Swift, and Y_{0M} for the Modified Voce. This confirms that based on the NLKH model, the yield surface does not

Table 13
Identification results for the TWIP980 for the case of one backstress component using the Swift and the Modified Voce hardening laws (two loading cycles).

Swift	C (MPa)	γ	Y_{0S}	ε_{0S}	n_S	/	CFV
Initial estimate	10,000	100	1000	0.1	0.1	/	
Identified	34,952	76.6	566	1.00	5.32×10^{-7}	/	6.61×10^8
Modified voce	C (MPa)	γ	Y_{0M} (MPa)	R_{0M}	R_{satM}	n_M	CFV
Initial estimate	10,000	100	1000	1000	100	10	
Identified	34,812	76.2	567	1.00×10^{-5}	1.00×10^{-5}	1.00×10^{-5}	6.62×10^8

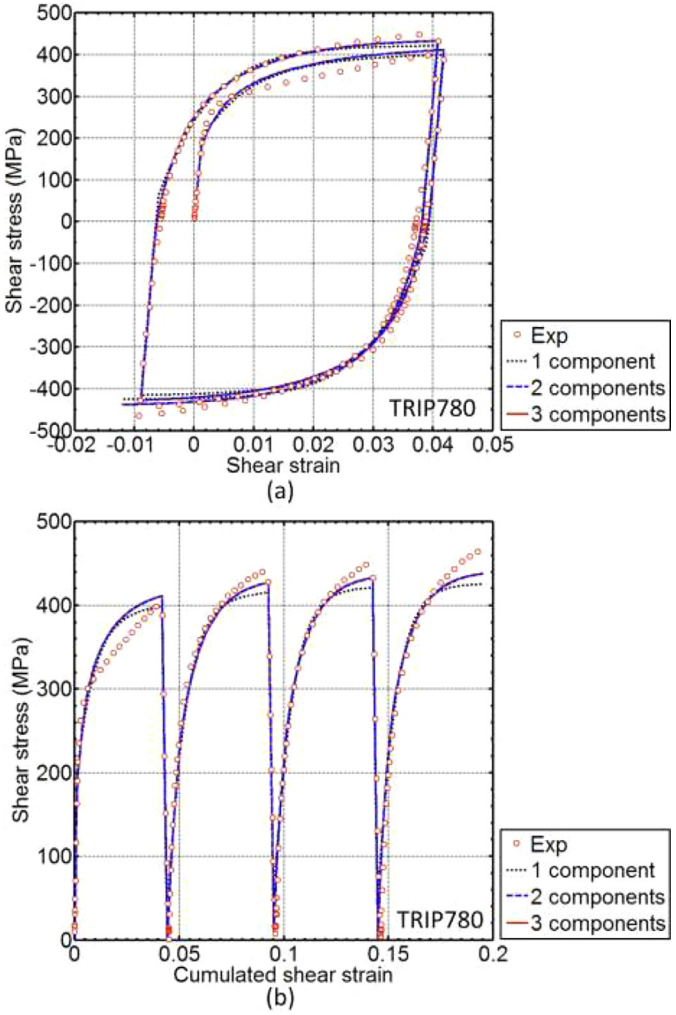

Fig. 9. Experimental and identified shear stress-strain curves for the TRIP780 in two cycles of forward-reverse simple shear obtained with Identified 1, plotted with respect to (a) true strain (b) cumulated strain.

expands but only translates during deformation for the selected TWIP980. Therefore, for the Voce hardening, R_{sat} and n were set to zero and one, respectively, and the identifications were performed again based on this. The results are given in Tables 14–16 for the cases of one, two, and three backstress components, respectively. It can be found that stable results were obtained with different initial estimates for all cases. The CFV is reduced from 6.62×10^8 to 3.12×10^8 when two components are used, and further reduced to 2.08×10^8 for the case of three components. One can see that the influence of three components is more significant for the TWIP980 than for the other two materials. The identified shear stress-shear strain curves are compared with the experimental counterpart in Fig. 10, and similar conclusions as for the DP600 and the TRIP780 can be drawn for the TWIP980.

Table 14
Identification results for the TWIP980 for the case of one backstress component when R_{sat} is set to zero (two loading cycles).

	C (MPa)	γ	Y_0 (MPa)	CFV
Initial estimate 1	10,000	100	100	
Identified 1	34,953	76.6	566	6.61×10^8
Initial estimate 2	50,000	500	500	
Identified 2	35,908	79.4	561	6.61×10^8

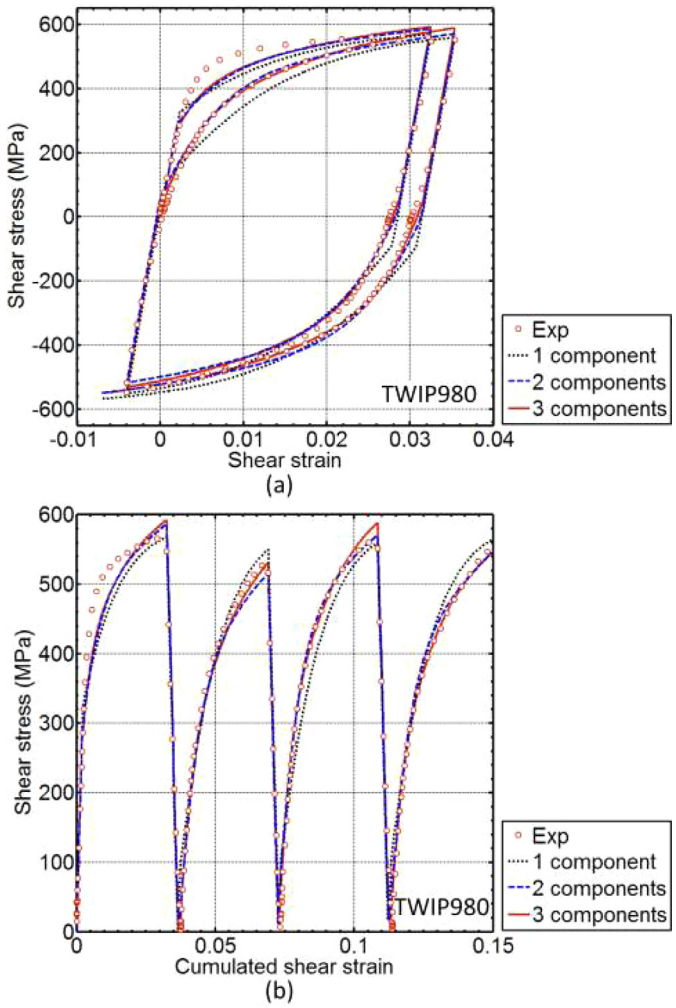

Fig. 10. Experimental and identified shear stress-strain curves for the TWIP980 in two cycles of forward-reverse simple shear obtained with Identified 1, plotted with respect to (a) true strain (b) cumulated strain.

It is worth noting that, in Figs. 9 and 10, for the TRIP780 and TWIP980, the identified curves show apparent deviation from their experimental counterparts, particularly in the first loading path (LP1). It is considered that the deviation is due to the lack of model robustness. The selected isotropic/kinematic hardening

Table 15
Identification results for the TWIP980 for the case of two backstress components when R_{sat} is set to zero (two loading cycles).

	C_1 (MPa)	γ_1	C_2 (MPa)	γ_2	Y_0 (MPa)	CFV
Initial estimate 1	20,000	200	2000	20	200	
Identified 1	61,348	193	7571	13.9	501	3.12×10^8
Initial estimate 2	80,000	100	8000	100	500	
Identified 2	62,205	200	8230	15.8	498	3.16×10^8

Table 16
Identification results for the TWIP980 for the case of three backstress components when Rsat is set to zero (two loading cycles).

	C_1 (MPa)	γ_1	C_2 (MPa)	γ_2	C_3 (MPa)	Y_0 (MPa)	CFV
Initial estimate 1	20,000	200	2000	20	200	200	
Identified 1	86,003	408	19,688	66.2	2474	472	2.08×10^8
Initial estimate 2	80,000	100	8000	100	500	500	
Identified 2	88,501	419	20,016	64.6	2408	466	2.06×10^8

models (with two and three backstress components) are not robust enough to characterize both the monotonic and reversal material behaviors for the TRIP780 and TWIP980 although they are suitable for describing the behavior of the DP600. The reason is not well understood, but it may be attributed to the difference in their material properties (material anisotropy, hardening behavior, etc.). This should be investigated further in the future. A more complex hardening model may decrease the deviation, which, however, is beyond the scope of the present work.

It should be mentioned that the proposed identification method is very computationally efficient. For the cases of one component, two components, and three components, the typical minimization time is only ~2 min, ~5 min, and ~5 min, respectively (with 32-bit operation system, 3.20 GHz CPU, and 8.00 GB RAM).

5. Conclusions

In this work, an identification method was proposed for the NLKH models combined with Voce isotropic hardening. This was implemented using the inverse solution tool, namely, the VFM. A global cost function that measures the quadratic gap between the IVW and the EVW was developed. By minimizing the cost function using the nonlinear least-square algorithm the unknown parameters were identified. The cases of one component, two components, and three components of the backstress have been studied, which also can be adapted to more components.

The proposed VFM scheme was validated on FE simulations of forward-reverse simple shear. The simulated strain and load data were accommodated in the VFM program and the input material parameters for the simulations retrieved successfully. It was found that, for the case of one backstress component, one forward-reverse loading cycle is sufficient to provide an accurate identification. Increasing a few loading cycles can slightly improve the identification accuracy. For the case of two components, two loading cycles are needed for an accurate identification. Gaussian white noise with the same amplitude as the current experimental measurements was added to the simulated strain data in order to evaluate the effect of noise on the identification accuracy. The results showed that the global error level was increased but within a tolerable range.

The experimental validation was implemented on the selected AHSS, namely, DP600, TRIP780 and TWIP980, which were tested under two cycles of forward-reverse simple shear. Reasonable and robust identification results were obtained for these materials regardless of different initial estimates. Specifically, it was found that for the TWIP980, based on the NLKH models, the yield surface only translates in stress space but does not expand. Thus, the identification was performed with the current yield stress defined as a constant value for the TWIP980. The shear stress-strain curves calculated using the identified parameters were compared with their experimental counterparts, showing good agreement. It was found that compared to the case of one backstress component, two components and three components provide a better fit of the material behavior, e.g., a better match between the identified shear stress-strain curve and its experimental counterpart. For all cases, the Bauschinger effect was well described by the identified curves. The proposed identification method is computationally efficient. A typical minimization time is only several minutes. Future work will be pursued to adapt this method to other NLKH models, e.g., the model that describes both the Bauschinger effect and the material anisotropy (Lee et al., 2007; Yoshida et al., 2015), in order to provide more identification options for the materials mechanics community.

Acknowledgments

The authors Dr. J. Fu, Prof. F. Barlat, and Dr. J.H. Kim are grateful for the financial support from POSCO. Prof. F. Pierron gratefully acknowledges support from the Royal Society and the Wolfson Foundation through a Royal Society Wolfson Research Merit Award.

Appendix A

The radial return algorithm developed by Sutton et al. (1996) is adopted to calculate stress increments from strain increments. The constitutive equation of elasticity is:

$$d\boldsymbol{\sigma} = \mathbf{Q} : d\boldsymbol{\varepsilon}_e \tag{A1}$$

where $d\boldsymbol{\sigma}$, $d\boldsymbol{\varepsilon}_e$, respectively, are the stress and elastic strain increment vector, $\mathbf{Q}$ is the stiffness matrix. This equation can be expressed as:

$$d\boldsymbol{\sigma} = \mathbf{Q} : (d\boldsymbol{\varepsilon} - d\boldsymbol{\varepsilon}_p) \tag{A2}$$

where $d\boldsymbol{\varepsilon}$, $d\boldsymbol{\varepsilon}_p$, respectively, are the total strain increment vector and the plastic part. For the following yield condition:

$$\mathcal{F} = \mathrm{f}(\boldsymbol{\sigma} - \boldsymbol{\alpha}) - \sigma_s(\varepsilon_p) = 0 \tag{A3}$$

with the associated flow rule:

$$d\boldsymbol{\varepsilon}_p = d\lambda \frac{\partial \mathcal{F}}{\partial \boldsymbol{\sigma}} \tag{A4}$$

and the consistency condition:

$$d\mathcal{F} = \frac{\partial \mathcal{F}}{\partial \boldsymbol{\sigma}} : d\boldsymbol{\sigma} + \frac{\partial \mathcal{F}}{\partial \varepsilon_p} d\varepsilon_p = 0 \tag{A5}$$

the elasto-plastic stress-strain relation can be derived as follows:

$$d\boldsymbol{\sigma} = \left(\mathbf{Q} - \frac{\mathbf{Q} : \frac{\partial \mathcal{F}}{\partial \boldsymbol{\sigma}} \otimes \mathbf{Q} : \frac{\partial \mathcal{F}}{\partial \boldsymbol{\sigma}}}{\frac{\partial \mathcal{F}}{\partial \boldsymbol{\sigma}} : \mathbf{Q} : \frac{\partial \mathcal{F}}{\partial \boldsymbol{\sigma}} - \frac{\partial \mathcal{F}}{\partial \varepsilon_p}} \right) : d\boldsymbol{\varepsilon} \tag{A6}$$

Appendix B

As introduced in Avril et al. (2010), Kim et al. (2013), in order to calculate the logarithmic strain values for the identification of material constitutive parameters using the proposed VFM program, the exact configuration of the specimen AOI is taken from ABAQUS® and meshed with triangular elements (here, 0.5 mm mesh size) using a Delaunay triangularization algorithm. In the undeformed state, for each triangular element, the nodal coordinates are known values since they are predefined in ABAQUS®. The coordinates of scattered data points inside each element are also known from DIC measurement. By fitting the scattered data points onto the nodal points, a basis of piecewise linear functions can be determined using the least squares regression. Using these piecewise functions and the coordinates of scattered points measured with DIC in the deformed states, the deformed nodal coordinates can be approximated. This method has an advantage that it enables the measurement of coordinates near edges, which are missing in DIC measurement. Then, the relationship between the undeformed nodal coordinates (x, y) and the deformed nodal coordinates (X, Y) can be expressed through a 2D affine transformation, which writes:

$$\begin{aligned} x &= a_1 + a_2 X + a_3 Y \\ y &= a_4 + a_5 X + a_6 Y \end{aligned} \tag{B1}$$

For each triangular element, six equations can be formed for the corresponding three element nodes according to Eq. (B1), by solving which the coefficients a_1 to a_6 can be calculated. The deformation gradient F in each element thus can be derived using the following equation with the assumption of plane stress state and the incompressibility condition $(\det(F) = 1)$.

$$F = \begin{bmatrix} \frac{\partial x}{\partial X} & \frac{\partial x}{\partial Y} & 0 \\ \frac{\partial y}{\partial X} & \frac{\partial y}{\partial Y} & 0 \\ 0 & 0 & \frac{1}{\frac{\partial x}{\partial X}\frac{\partial y}{\partial Y} - \frac{\partial x}{\partial Y}\frac{\partial y}{\partial X}} \end{bmatrix} = \begin{bmatrix} a_2 & a_3 & 0 \\ a_5 & a_6 & 0 \\ 0 & 0 & \frac{1}{a_2 a_6 - a_3 a_5} \end{bmatrix} \tag{B2}$$

Finally, the logarithmic strain can be determined from the deformation gradient F through the left stretch tensor $B = \sqrt{FF^T}$ using the equation:

$$\varepsilon_{ln} = \sum_{k=1}^{3} ln(\lambda_k) r_k \otimes r_k \tag{B3}$$

where λ_k and r_k, respectively, are the eigenvalues and the eigenvectors of the left stretch tensor B.

References

Armstrong, P.J., Frederick, C.O., 1966. A Mathematical Representation of the Multiaxial Bauschinger Effect. Central Electricity Generating Board [and] Berkeley Nuclear Laboratories, Research & Development Dept.

Avril, S., Badel, P., Duprey, A., 2010. Anisotropic and hyperelastic identification of in vitro human arteries from full-field optical measurements. J. Biomech. 43, 2978–2985.

Avril, S., Bonnet, M., Bretelle, A.S., Grédiac, M., Hild, F., Ienny, P., Latourte, F., Lemosse, D., Pagano, S., Pagnacco, E., Pierron, F., 2008. Overview of identification methods of mechanical parameters based on full-field measurements. Exp. Mech. 48, 381–402.

Barlat, F., Gracio, J.J., Lee, M.-G., Rauch, E.F., Vincze, G., 2011. An alternative to kinematic hardening in classical plasticity. Int. J. Plast. 27, 1309–1327.

Barlat, F., Ha, J., Grácio, J.J., Lee, M.-G., Rauch, E.F., Vincze, G., 2013. Extension of homogeneous anisotropic hardening model to cross-loading with latent effects. Int. J. Plast. 46, 130–142.

Barlat, F., Vincze, G., Grácio, J.J., Lee, M.G., Rauch, E.F., Tomé, C.N., 2014. Enhancements of homogenous anisotropic hardening model and application to mild and dual-phase steels. Int. J. Plast. 58, 201–218.

Broggiato, G., Campana, F., Cortese, L., 2008. The Chaboche nonlinear kinematic hardening model: calibration methodology and validation. Meccanica 43, 115–124.

Chaboche, J.L., 1986. Time-independent constitutive theories for cyclic plasticity. Int. J. Plast. 2, 149–188.

Chaboche, J.L., 2008. A review of some plasticity and viscoplasticity constitutive theories. Int. J. Plast. 24, 1642–1693.

Chalal, H., Avril, S., Pierron, F., Meraghni, F., 2006. Experimental identification of a nonlinear model for composites using the grid technique coupled to the virtual fields method. Composit. Part A 37, 315–325.

Chaparro, B.M., Thuillier, S., Menezes, L.F., Manach, P.Y., Fernandes, J.V., 2008. Material parameters identification: gradient-based, genetic and hybrid optimization algorithms. Comput. Mater. Sci. 44, 339–346.

Choi, J.S., Lee, J.W., Kim, J.H., Barlat, F., Lee, M.G., Kim, D., 2015. Measurement and modeling of simple shear deformation under load reversal: application to advanced high strength steels. Int. J. Mech. Sci. 98, 144–156.

Chongthairungruang, B., Uthaisangsuk, V., Suranuntchai, S., Jirathearanat, S., 2012. Experimental and numerical investigation of springback effect for advanced high strength dual phase steel. Mater. Des. 39, 318–328.

Chung, K., Lee, M.-G., Kim, D., Kim, C., Wenner, M.L., Barlat, F., 2005. Spring-back evaluation of automotive sheets based on isotropic-kinematic hardening laws and non-quadratic anisotropic yield functions: Part I: theory and formulation. Int. J. Plast. 21, 861–882.

Chung, K., Ma, N., Park, T., Kim, D., Yoo, D., Kim, C., 2011. A modified damage model for advanced high strength steel sheets. Int. J. Plast. 27, 1485–1511.

Collin, J.-M., Parenteau, T., Mauvoisin, G., Pilvin, P., 2009. Material parameters identification using experimental continuous spherical indentation for cyclic hardening. Comput. Mater. Sci. 46, 333–338.

Creath, K., 1985. Phase-Shifting Speckle Interferometry, pp. 337–346.

Dafalias, Y.F., Popov, E.P., 1975. A model of nonlinearly hardening materials for complex loading. Acta Mech. 21, 173–192.

Eggertsen, P.-A., Mattiasson, K., 2010. On the identification of kinematic hardening material parameters for accurate springback predictions. Int J Mater. Form 4, 103–120.

Farhat, C., Hemez, F.M., 1993. Updating finite element dynamic models using an element-by-element sensitivity methodology. AIAA J. 31, 1702–1711.

Frederick, C.O., Armstrong, P.J., 2007. A mathematical representation of the multiaxial Bauschinger effect. Mater. High Temp. 24, 1–26.

Fu, J., Barlat, F., Kim, J.-H., Pierron, F., 2016. Application of the virtual fields method to the identification of the homogeneous anisotropic hardening parameters for advanced high strength steels. Int. J. Plast. doi:10.1016/j.ijplas.2016.07.013.

Geng, L., Wagoner, R.H., 2002. Role of plastic anisotropy and its evolution on springback. Int. J. Mech. Sci. 44, 123–148.

Grédiac, M., Pierron, F., 2006. Applying the virtual fields method to the identification of elasto-plastic constitutive parameters. Int. J. Plast. 22, 602–627.

Grédiac, M., Sur, F., Blaysat, B., 2016. The grid method for in-plane displacement and strain measurement: a review and analysis. Strain. 52, 205–243.

Güner, A., Soyarslan, C., Brosius, A., Tekkaya, A.E., 2012. Characterization of anisotropy of sheet metals employing inhomogeneous strain fields for Yld2000-2D yield function. Int. J. Solids Struct. 49, 3517–3527.

Kim, J.H., Serpantié, A., Barlat, F., Pierron, F., Lee, M.G., 2013. Characterization of the post-necking strain hardening behavior using the virtual fields method. Int. J. Solids Struct. 50, 3829–3842.

Lee, M.-G., Kim, D., Kim, C., Wenner, M.L., Wagoner, R.H., Chung, K., 2005a. Spring-back evaluation of automotive sheets based on isotropic-kinematic hardening laws and non-quadratic anisotropic yield functions: Part II: characterization of material properties. Int. J. Plast. 21, 883–914.

Lee, M.-G., Kim, D., Kim, C., Wenner, M.L., Wagoner, R.H., Chung, K., 2007. A practical two-surface plasticity model and its application to spring-back prediction. Int. J. Plast. 23, 1189–1212.

Lee, M.G., Kim, D., Kim, C., Wenner, M.L., Chung, K., 2005b. Spring-back evaluation of automotive sheets based on isotropic-kinematic hardening laws and non-quadratic anisotropic yield functions, part III: applications. Int. J. Plast. 21, 915–953.

Mahmoudi, A.H., Pezeshki-Najafabadi, S.M., Badnava, H., 2011. Parameter determination of Chaboche kinematic hardening model using a multi objective genetic algorithm. Comput. Mater. Sci. 50, 1114–1122.

Manopulo, N., Barlat, F., Hora, P., 2015. Isotropic to distortional hardening transition in metal plasticity. Int. J. Solids Struct. 56–57, 11–19.

Narasimhan, N., Lovell, M., 1999. Predicting springback in sheet metal forming: an explicit to implicit sequential solution procedure. Finite Elem. Anal. Des. 33, 29–42.

Notta-Cuvier, D., Langrand, B., Markiewicz, E., Lauro, F., Portemont, G., 2013. Identification of Johnson–Cook's viscoplastic model parameters using the virtual fields method: application to titanium alloy Ti6Al4V. Strain 49, 22–45.

Ohno, N., Wang, J.D., 1993. Kinematic hardening rules with critical state of dynamic recovery, part I: formulation and basic features for ratchetting behavior. Int. J. Plast. 9, 375–390.

Oliveira, M.C., Alves, J.L., Chaparro, B.M., Menezes, L.F., 2007. Study on the influence of work-hardening modeling in springback prediction. Int. J. Plast. 23, 516–543.

Omerspahic, E., Mattiasson, K., Enquist, B., 2006. Identification of material hardening parameters by three-point bending of metal sheets. Int. J. Mech. Sci. 48, 1525–1532.

Pierron, F., Avril, S., Tran, V.T., 2010a. Extension of the virtual fields method to elasto-plastic material identification with cyclic loads and kinematic hardening. Int. J. Solids Struct. 47, 2993–3010.
Pierron, F., Grediac, M., 2012, Springer Science & Business Media. The Virtual Fields Method: Extracting Constitutive Mechanical Parameters From Full-Field Deformation Measurements.
Pierron, F., Sutton, M.A., Tiwari, V., 2010b. Ultra high speed dic and virtual fields method analysis of a three point bending impact test on an aluminium bar. Exp. Mech. 51, 537–563.
Post, D., Baracat, W.A., 1981. High-sensitivity moiré interferometry-A simplified approach - Superior results are obtained with simplified equipment and techniques. Exp. Mech. 21, 100–104.
Prager, W., 1949. Recent developments in the mathematical theory of plasticity. J. Appl. Phys. 20, 235–241.
Rezaiee-Pajand, M., Sinaie, S., 2009. On the calibration of the Chaboche hardening model and a modified hardening rule for uniaxial ratcheting prediction. Int. J. Solids Struct. 46, 3009–3017.
Roux, E., Bouchard, P.O., 2015. On the interest of using full field measurements in ductile damage model calibration. Int. J. Solids Struct. 72, 50–62.
Sutton, M.A., Deng, X., Liu, J., Yang, L., 1996. Determination of elastic-plastic stresses and strains from measured surface strain data. Exp. Mech. 36, 99–112.
Sutton, M.A., Orteu, J.-J., Schreier, H., 2009. Image Correlation for Shape, Motion and Deformation Measurements: Basic Concepts,Theory and Applications. Springer Publishing Company Incorporated.
Yin, Q., Soyarslan, C., Güner, A., Brosius, A., Tekkaya, A.E., 2012. A cyclic twin bridge shear test for the identification of kinematic hardening parameters. Int. J. Mech. Sci. 59, 31–43.
Yoshida, F., Hamasaki, H., Uemori, T., 2015. Modeling of anisotropic hardening of sheet metals including description of the Bauschinger effect. Int. J. Plast. 75, 170–188.
Yoshida, F., Uemori, T., 2002. A model of large-strain cyclic plasticity describing the Bauschinger effect and workhardening stagnation. Int. J. Plast. 18, 661–686.
Yoshida, F., Urabe, M., Hino, R., Toropov, V.V., 2003. Inverse approach to identification of material parameters of cyclic elasto-plasticity for component layers of a bimetallic sheet. Int. J. Plast. 19, 2149–2170.
Zang, S.-l., Lee, M.-G., Sun, L., Kim, J.H., 2014. Measurement of the Bauschinger behavior of sheet metals by three-point bending springback test with pre-strained strips. Int. J. Plast. 59, 84–107.
Zhang, S., Leotoing, L., Guines, D., Thuillier, S., Zang, S.-l., 2014. Calibration of anisotropic yield criterion with conventional tests or biaxial test. Int. J. Mech. Sci. 85, 142–151.
Zhao, K.M., Lee, J.K., 2002. Finite element analysis of the three-point bending of sheet metals. J. Mater. Process. Technol. 122, 6–11.
Ziegler, H., 1959. A modification of Prager's hardening rule. Q. Appl. Math.